Impact of permeability evolution in igneous sills on hydrothermal flow and hydrocarbon transport in volcanic sedimentary basins

Ole Rabbel[1*], Christophe Y. Galerne[2], Jörg Hasenclever[3], Olivier Galland[1], Karen Mair[1], Octavio Palma[4]

[1] NJORD, University of Oslo, P.O. 1048 Blindern, 0316 Oslo, Norway

[2] Faculty of Geosciences, University of Bremen, Klagenfurter Straße 2-4, 28359 Bremen, Germany

[3] Institute of Geophysics, Center for Earth System Research and Sustainability, University of Hamburg Bundesstrasse 55, 20146 Hamburg, Germany

[4] Facultad de Ciencias Naturales y Museo, Universidad de La Plata, Paseo del Bosque s/no - B1900FWA – La Plata, Argentina

*Corresponding author, e-mail: ole.rabbel@gmail.com

15 **Abstract:**

16 Sill intrusions emplaced in organic-rich sedimentary rocks trigger the generation and

17 migration of hydrocarbons in volcanic sedimentary basins. Based on seismic and geological

18 observations, numerical modeling studies of hydrothermal flow around sills have shown that

19 thermogenic methane is channeled towards the intrusion tip, where it rises to the surface in a

20 hydrothermal vent. However, these models typically assume impermeable sills and ignore

21 potential effects of permeability evolution in cooling sills, e.g., due to fracturing. To address

22 this issue, we combine a geological field study of a volcanic basin (Neuquén Basin,

23 Argentina) with hybrid FEM/FVM numerical modeling of hydrothermal flow around a sill,

24 including hydrocarbon generation and transport. Our field observations show that graphitized

25 bitumen veins and cooling joints filled with solid bitumen or fluidized shale are common

26 within the studied sills. Raman spectroscopy indicates graphitization at temperatures between

27 350-500°C, evidencing fluid flow within the intrusions shortly after solidification. This

28 finding motivates our modeling study, which investigates flow patterns around intrusions that

29 become porous and permeable upon solidification. The results show three distinct flow

30 phases affecting the transport of hydrocarbons generated in the contact aureole: (1) Contact-

31 parallel flow toward the sill tip before solidification, (2) upon complete solidification, sudden

32 vertical "flushing" of overpressured hydrocarbon-rich fluids from the lower contact aureole

33 through the hot sill, and (3) slow rise of hydrocarbon-rich fluids above the sill center, and

34 backward-downward flow near the sill tip. We conclude that permeability creation within

35 cooling sills may be an important factor for hydrothermal flow and hydrocarbon transport in

36 volcanic basins, as it considerably alters the fluid pressure configuration and flow patterns by

37 dissipating overpressure below the sills. This could, for instance, lead to a reduced potential

38 for hydrothermal venting.

39

1 Introduction

40

41 Sill intrusions emplaced in sedimentary rocks strongly influence the generation and migration

42 of hydrocarbons and greenhouse gases in volcanic sedimentary basins. If sill intrusions are

43 emplaced in organic-rich strata, they trigger contact-metamorphic reactions (e.g., organic

44 matter transformation), overpressure generation, and hydrothermal fluid flow in the

45 surrounding strata (Einsele et al., 1980; Aarnes et al., 2012). Many recent studies of volcanic

46 sedimentary basins investigate how such processes may cause the formation of hydrothermal

47 vent complexes, which facilitate greenhouse gas release to the atmosphere and can thus drive

48 global climate change (Svensen et al., 2004; Aarnes et al., 2010; Aarnes et al., 2012; Iyer et

49 al., 2013; Iyer et al., 2017; Galerne and Hasenclever, 2019). Additionally, the same processes

50 can be critical factors for hydrocarbon generation and migration in igneous petroleum

51 systems containing sills emplaced within shale formations (Senger et al., 2017; Spacapan et

52 al., 2020).

53 Hydrothermal flow in response to the intrusion of magma into sedimentary host rocks has

54 been investigated for decades. The magmatic heat input leads to several temperature-

55 dependent processes that promote strong fluid pressure increase, which drive fluid flow

56 (Einsele et al., 1980; Delaney, 1982). These processes include for instance thermal fluid

57 expansion, mineral dehydration, organic matter transformation into hydrocarbon generation,

58 and pore space reduction due to mineral precipitation (Einsele et al., 1980; Delaney, 1982;

59 Aarnes et al., 2010; Townsend, 2018). When the rate of overpressure generation is larger than

60 flow-driven pressure dissipation, e.g. in low-permeable rocks like shale, hydraulic fractures

61 form and locally enhance fluid flow and pressure release (Aarnes et al., 2012; Kobchenko et

62 al., 2014; Panahi et al., 2018; Rabbel et al., 2020). This process may lead to explosive

63 hydrothermal vents, which are present in several volcanic basins (Nermoen et al., 2010;

64 Aarnes et al., 2012; Iyer et al., 2017).

65 Numerical models simulate these coupled processes to understand hydrothermal flow

66 dynamics and the associated hydrocarbon migration (usually represented as methane carried

67 in the hydrothermal fluids), typically in the context of vent formation around sills emplaced

68 in organic-rich sediments. Such simulations assume that sills are impermeable and show that

69 vents seem to preferentially form at the inclined tips of large "saucer-shaped" sills because

70 this situation favours both fast fluid pressure build-up below the sills and focussed fluid

71   migration towards the tips (Iyer et al., 2013, Iyer et al., 2017; Galerne and Hasenclever,

72   2019).

73   However, observations from several volcanic sedimentary basins indicate that the assumption

74   of impermeable sills is not generally valid. Sills often host fracture networks including

75   different fracture types. These form shortly after solidification of the magma and may include

76   columnar cooling joints or fractures related to hydraulic fracturing during hydrothermalism

77   (Senger et al. 2015, Witte et al. 2012, Rabbel et al., 2021). Multiple studies have provided

78   evidence that such fracture networks may be open and can contain water (Chevallier et al.,

79   2004) or hydrocarbons and act as fluid pathways or even fractured reservoirs (Mark et al.,

80   2018; Schofield et al., 2020; Spacapan et al., 2020). However, it is currently unknown to

81   which extent the generation of fractures during the cooling phase of sills affects hydrothermal

82   flow and associated hydrocarbon migration in volcanic basins.

83   To address this issue, we present a geological case study from the northern Neuquén Basin,

84   Argentina, combined with numerical hydrothermal simulations. The northern Neuquén Basin

85   provides particularly well-documented examples of sills with extensive cooling joint

86   networks emplaced in organic-rich shale because the fractured sills represent the main

87   reservoirs in several commercially producing oil fields (Rodriguez Monreal et al., 2009;

88   Witte et al., 2012; Spacapan et al., 2020). Additionally, numerical modeling and subsurface

89   data demonstrate the strong thermal impact of intrusions on host rock maturation in these

90   systems (Rodriguez Monreal et al., 2009; Spacapan et al., 2018). We first present geological

91   evidence from outcropping sills to provide evidence for hydrocarbon transport through

92   fractured sills in a hydrothermal environment. Our field observations motivate the

93   implementation of numerical modelling to test the influence of cooling joint formation, i.e.

94   permeable sills, on the hydrothermal flow patterns and hydrocarbon migration. We performed

95   a parameter study, in which we test this effect for sills of varying thickness and emplacement

96   depth. By integrating the simulation results with geological evidence, we show how

97   permeable sills affect hydrothermal flow in volcanic sedimentary basins as well as the fate of

98   hydrocarbons generated by contact metamorphism.

99

2 Geological observations

2.1 Geological setting

The study area is located around the Río Grande Valley (RGV) in the northern Neuquén
Basin, Argentina, about 100 km south of the town of Malargüe (Figure 1). The Neuquén Basin
initially formed as a series of isolated half-grabens during the late Triassic to early Jurassic
(Howell et al., 2005). During the middle Jurassic to early Cretaceous, these depocenters
coalesced during thermal subsidence, forming a large shallow-marine basin. This phase
included the deposition of the Vaca Muerta and Agrío formations, which comprise several
hundreds of meters of calcareous, organic-rich shale and form two important source rock
formations for presently exploited petroleum systems (Kietzmann et al., 2014). From the
early Cretaceous, the basin developed into a foreland basin in response to the compressive
tectonic regime of the Andean orogeny. This led to inversion of the Triassic normal faults and
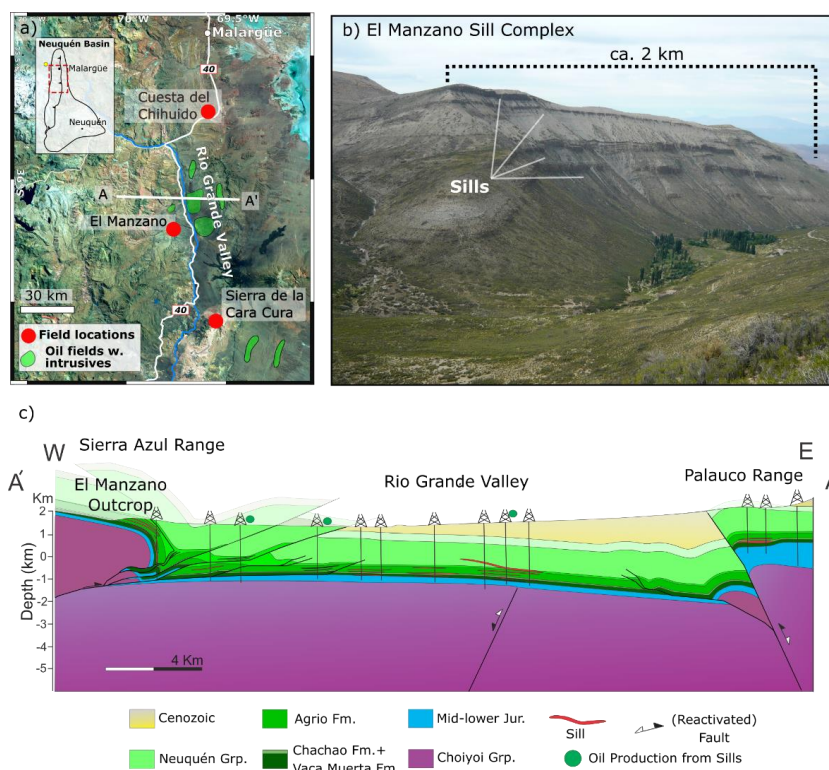
Figure 1. (a) Satellite image of the study area in the northern Neuquén Basin including field localities (red
dots) and producing igneous petroleum systems (green areas). (b) View of the El Manzano sill complex
outcrop in the Sierra Azul range (Photo: F. Soto). (c) E-W structural geological section illustrating the
relation between subsurface and outcropping sill complexes (courtesy. J. B. Spacapan)

112 generation of a series of fold-thrust belts along the western basin boundary (Manceda and

113 Figueroa, 1995; Yagupsky et al., 2008).

114 In addition to tectonic deformation, the northern Neuquén Basin experienced intense

115 magmatic activity that formed a series of volcanic plateaus and widespread magmatic

116 intrusions within the sedimentary succession (Kay et al., 2006). In the study area, two main

117 eruptive cycles, termed Molle and Huincán eruptive cycles, occurred in the late Oligocene-

118 mid Miocene and the late Miocene-Pleistocene, respectively (Combina and Nullo, 2005).

119 These events lead to the emplacement of extensive andesitic and basaltic sill complexes

120 predominantly in the Vaca Muerta and Agrío Formations, but also in overlying gypsum and

121 sandstone units (Spacapan et al., 2020).

122 In the RGV, heavily fractured sills emplaced in the Vaca Muerta and Agrío formations

123 constitute the reservoirs in an actively producing igneous petroleum system (Schiuma, 1994;

124 Witte et al., 2012). Spacapan et al. (2020) reported 2 to 27 m thick sills in these shale

125 formations, but up to 54 m within shallower clastic sediments of RGV. Other studies from the

126 northern Neuquén Basin report thick laccolith intrusions (>100 m) acting as reservoirs

127 (Rodriguez Monreal et al., 2009). Spacapan et al. (2018) showed that the heat input provided

128 by the sills matured the Vaca Muerta and Agrío shale formations, which otherwise show very

129 low thermal maturity at burial depths of ca. 2-2.5 km. The established model for the

130 formation of these igneous reservoirs includes that the intrusions developed interconnected

131 cooling joint networks, which subsequently stored the generated hydrocarbons (Witte et al.,

132 2012; Spacapan et al., 2020).

133 In addition to the subsurface sill complexes, thrust tectonics brought to surface exceptional

134 outcrop analogues in the surrounding mountain ranges including the Sierra Azul, Sierra Cara

135 Cura, and Cuesta del Chihuido (Figure 1). Several studies describe these localities, which

136 offer easy access to sills emplaced in the Vaca Muerta and Agrio formations (Spacapan et al.,

137 2017; Rabbel et al., 2018; Rabbel et al., 2021). Especially the km-scale outcrops at El

138 Manzano (Figure 1b) and Sierra Cara Cura constitute direct analogues to the subsurface sill

139 complexes of the RGV igneous petroleum system (Palma et al., 2019; Rabbel et al., 2021).

140 These three field localities are ideal case studies to reveal the interactions between igneous

141 intrusions and the petroleum system.

142

2.2 Field methods

The fieldwork conducted for this study aims to document evidence of hydrothermal flow and hydrocarbon transport related to permeable intrusions in the study area. During three field campaigns, we collected an extensive dataset at the outcrops in El Manzano, Sierra de la Cara Cura, and Cuesta del Chihuido (Figure 1). We gathered ground-based and drone digital photographs to document outcrop observations. Additionally, we collected over 100 rock samples from the intrusions, surrounding shale as well as various types of veins for geochemical analyses. Here, we focus on presenting field evidence for hydrothermal flow of hydrocarbon-bearing fluids both around and within the sills, which then motivates the numerical study. Note that a more comprehensive description of the field study is presented by Rabbel et al. (2021).

2.3 Observations of hydrocarbons inside and around sills

Outcropping sills in all three localities feature solid bitumen and black shale inside the fracture network of the sills. At Cuesta del Chihuido, both the side and roof of thin sills are exposed, and the side view reveals upwelling dykelets of black shale (Vaca Muerta Formation) entering the sill from the bottom contact (Figure 2a). The top view of the same sill shows the entire polygonal cooling joint network with a black fill of the same material (Figure 2b). Brecciated igneous material often surrounds the dykelets where they enter the intrusion.

The larger sills at El Manzano (Sierra Azul) and Sierra Cara Cura also show widespread bitumen in the fracture network of the sills, but at a much larger scale (Figure 3). We observe arrays of 1-up to 50 cm thick and >10 m high bitumen dykes or veins (Figure 3a). Here, the bitumen dyke cuts across the contact aureole and enters the sill intrusion. We find exposures of similar structures where the sill interior is accessible (Figure 3b). The sill appears heavily fractured in addition to preexisting cooling joints, and solid bitumen or calcite fill nearly all fractures. On closer inspection, the bituminous material in these veins has a shiny and fibrous texture.

At an exposed sill tip at El Manzano, we also observe that thick bitumen veins appear to be concentrated along the tip contact, where they mutually cross-cut with calcite veins of at least similar thicknesses (Figure 3c,d). These calcite veins have cm-scale pores, which occasionally

174   contain solid bitumen themselves and release a strong hydrocarbon smell when the vein is

175   broken up.

176

177   **2.4   Bitumen characterization**

178   The fibrous texture of the observed bitumen within the sills is intriguing and suggests that it

179   partly experienced graphitization, i.e. it is much higher-grade bituminous material than that

180   described in the Neuquén basin by Cobbold et al. (1999) and Zanella et al. (2015).

181   In the field, we tested this hypothesis by measuring the resistivity of the fibrous bitumen with

182   a hand-held multimeter. Graphitization of bitumen significantly changes the electric

183   resistivity of the material: amorphous solid bitumen is very resistive and used as an electric

184   insulator in industry applications (Hays et al., 1967), while graphite is an excellent conductor.

185   Qualitative on-site resistivity measurements showed that the fibrous bitumen conducts

186   electric currents well, i.e., within the detection limit of a standard multimeter, suggesting

187   significant graphitization.

188   In addition, we applied Raman spectroscopy to better constrain the nature of the solid

189   bitumen and its thermal history. Raman spectroscopy provides positions and relative

190   intensities of spectral peaks characterizing carbonaceous materials like bitumen, including D

191   ("disorder") and G ("graphite") peaks at 1345 cm^{-1} and 1585 cm^{-1}, respectively (Potgieter-

192   Vermaak et al., 2011; Rantitsch et al., 2016). The shape of the spectra and the D/G peak and

193   area ratios allow classification of high-grade alteration of the bitumen to anthracite or (semi-

194   )graphite and may serve as a geothermometer for high-temperature regimes (Beyssac et al.,

195   2002; Rantitsch et al., 2016). Due to the high temperatures within and around igneous

196   intrusions, we expect this method to indicate the degree of thermal alteration and thus

197   temperatures that the hydrocarbons experienced. Since Raman spectra can show varying

198   absolute intensities, we normalized each spectrum to the intensity of the respective G peak

199   (I_G) for visualization purposes.

200

201
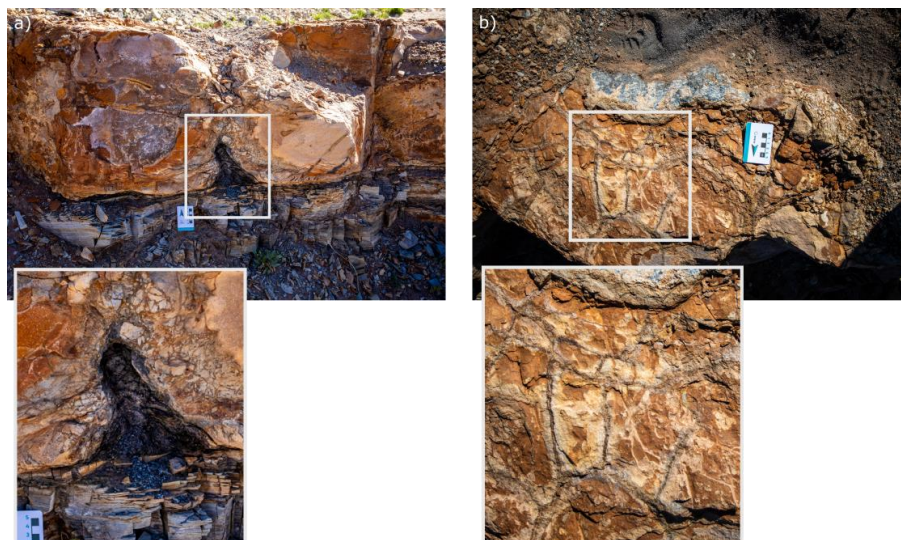
Figure 2. Field observations of upwelling dykelets of liquefied shale and bitumen entering the cooling joint network of a thin sill at Cuesta del Chihuido (ca. 30 cm thick). (a) Side view showing the sediment-intrusion contact and dyke (Photo: D. Michelon), (b) top view demonstrating black bituminous fill in the polygonal cooling joints.

202

203   Raman spectrograms of the sampled bitumen veins show very clearly developed G and D1

204   peaks and I_{D1}/I_G ratios of 0.6 and 0.9, respectively. The D3 band between the peaks is nearly

205   absent in the sample from Sierra de la Cara Cura, while it is visible at low intensity in the

206   presented sample from El Manzano (Figure 4).
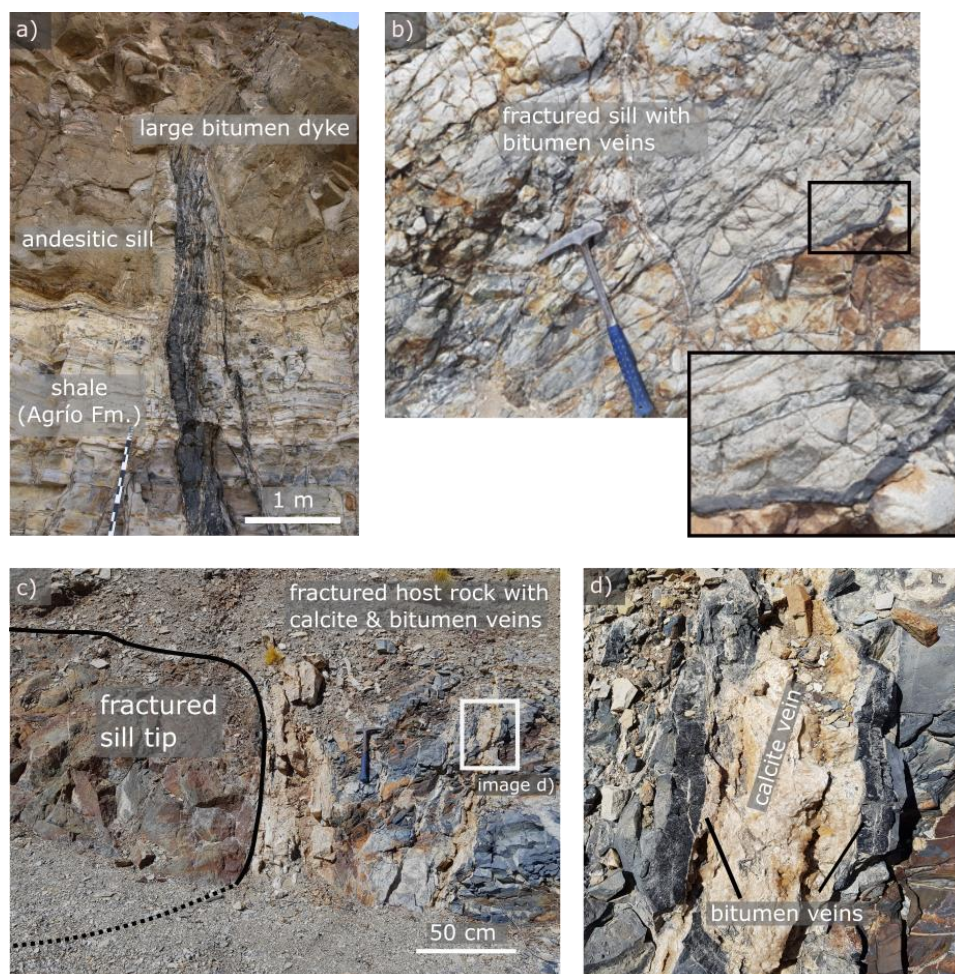
Figure 3. Examples of dykes or veins of solid bitumen associated the sill intrusions. (a) Bitumen dyke at El Manzano of >10 m height and up to 0.5 m thickness originating in the aureole of Agrío Fm. and entering the sill through the bottom contact. (b) Fractured zone inside a sill at Sierra de la Cara Cura exhibiting many cm-scale veins of solid bitumen. (c, d) Exposed sill tip at El Manzano showing high concentration of fibrous bitumen and calcite veins in the contact in front of the tip.

2.5 Composition and thermal implications of bitumen samples

207

208   We compare our Raman results with those measured in carbonaceous material from several

209   studies, where increased graphitization and metamorphism lead to well-developed, narrow

210   graphite (G) and disordered carbon (D1) peaks, weak or absent D3 bands, and I_G/I_D peak

211   ratios of <1 (Beyssac et al., 2002; Kwiecinska et al., 2010; Rantitsch et al., 2016). Although

212   we did not perform quantification via peak-fitting, a qualitative comparison of our results

213   with highly metamorphosed sediments presented by Beyssac et al. (2002, Fig. 6 and 11

214   therein) leads to estimated temperatures of 350-500°C for our samples (Figure 4).

215   Hydrothermal graphitization can occur along intrusion-sediment contacts at relatively

216   shallow crustal levels and requires temperatures of >= 400°C (Buseck and Beyssac, 2014).

217   Hydraulic fracturing focuses the flow of hydrothermal fluids oversaturated with CH_4 and/or

218   CO_2 from which crystalline graphite may precipitate (Rumble, 2014). This fits well with the

219   observations that the bitumen dykes in our study area consist of pure, often crystalline

220   graphitic material and occupy fractured zones in the aureole, around the tip, or within the sills

221   themselves (Figure 3). In a previous summary of fracture types present in the sills of the study

222   area, Rabbel et al. (2021) interpreted these features as hydraulic fractures. Thus, evidence

223   from graphitized bitumen in the fractures in the aureole and the sills themselves points to

224   hydrocarbon transport in a high-pressure, high-temperature environment in which at least part

225   of the mobilized carbon transforms to graphitic carbonaceous material.

226   Our field and sample results strongly suggest that significant volumes of hydrocarbons

227   circulated through the sills when the temperature at their margins was 350-500°C. The

228   temperature was thus likely much higher in the interior of the sills. We infer that

229   hydrothermal flow also occurred along cooling fractures within the sill, i.e., the sill developed

230   some permeability while still hot (cf. Figure 2). This interpretation challenges the

231   assumptions of previous models of hydrothermal circulation around cooling sills, in which

232   the sills remain impermeable during cooling (Aarnes et al., 2012; Iyer et al., 2017, Galerne &

233   Hasenclever, 2019). To which extent permeability creation within hot sills affects

234   hydrothermal flow and the associated hydrocarbon transport around sills is not known. In the

235   following section, we therefore present numerical simulations to test the effects of

236   permeability increase associated with fracturing within the sills on hydrothermal circulations,

237   and how this affects hydrothermal transport of hydrocarbons around sills.

238

239

240
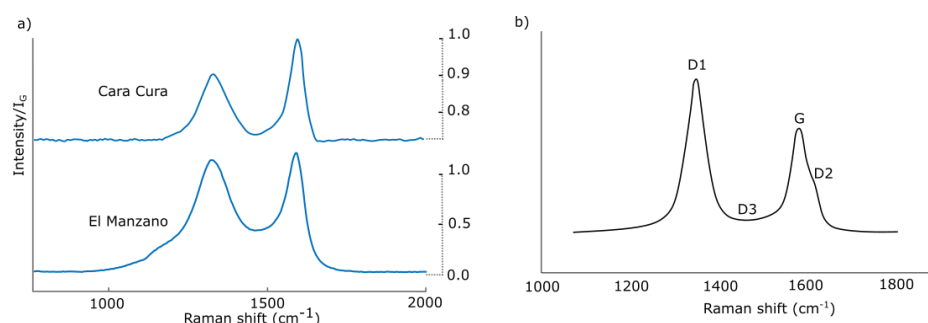
Figure 4. (a) Raman spectra from two bitumen vein samples at Sierra de la Cara Cura and El Manzano, respectively. Both samples include well-developed and narrow graphite and disordered carbon (G, D1) peaks as well as weak or absent D3 band. (b) Reference Raman spectrum to illustrate spectra decomposition of carbonaceous material after Beyssac et al. (2002).

241 **3   Numerical Simulations**

242 **3.1   Model description**

243 We employ the two-dimensional (2D) finite element model of Galerne and Hasenclever

244 (2019), who applied it to quantify degassing through sill-related hydrothermal vents. As this

245 complex model is presented in detail in Galerne and Hasenclever (2019), we will limit our

246 discussion to the main features and point out the key adjustments for this study. In short, the

247 model simulates hydrothermal flow around a cooling sill but is also coupled to a model for

248 the heat-driven chemical transformation of organic matter into hydrocarbons (represented by

249 methane). This allows us to investigate not only hydrothermal circulation around sills as such

250 but also how this affects the transport of the hydrocarbons generated in the aureole.

251 The model considers single-phase hydrothermal flow of a compressible fluid in a porous

252 medium following Darcy's law. Temperature calculations comprise heat diffusion, heat

253 advection and heat sources/sinks related to latent heat of magma crystallization, dehydration,

254 thermal cracking of organic matter as well as internal fluid friction and pressure-volume

255 work. Fluid density varies with temperature and pressure according to the equation of state of

256 pure water. The pore pressure equation also contains source terms representing fluid release

257 due to temperature-dependent, irreversible contact metamorphic reactions, including (i)

258 organic matter transformation into methane and (ii) clay mineral dehydration.

259 To calculate organic matter transformation to methane, the model uses the EASY%Ro

260 method (Sweeney and Burnham, 1990), which quantifies the converted fraction of organic

261   matter and thermal maturity through vitrinite reflectance *Ro*. We monitor transport and

262   accumulation of the released methane due to hydrothermal flow using a finite volume

263   advection scheme, but do not consider buoyancy effects resulting from the addition of

264   methane to the pore fluid. Clay mineral dehydration follows the maximum storable weight

265   fraction of water in the stable mineral assemblage at a given temperature, which is predicted

266   by phase equilibria (Connolly, 2009). This process not only produces additional pore fluid,

267   but also causes a permanent porosity increase in the affected host rock to ensure mass

268   conservation of rock and fluid. Note here that while the model uses the properties of methane,

269   the results can be used to understand transport of (light) hydrocarbons around sills in general.

270   We thus use "methane" and "hydrocarbons" interchangeably in the context of this study.

271   The model provides time series of the 2D fields of all relevant rock properties in the model

272   domain and physical quantities related to metamorphism and hydrothermal flow. Since we

273   investigate the impact of permeable sills on the fluid and hydrocarbon circulation, our

274   analysis focuses on visualization of the flow fields and methane accumulation during cooling.

275   **3.2   Adjustments for this study**

276   We adjusted two aspects of the original model to honor geological observations in the study

277   area. First, we limit the permeability increase in the host rock due to rock fracturing to tensile

278   hydraulic fracturing, but do not consider shear failure. At sufficiently high pore fluid

279   overpressure, i.e., if pore pressure exceeds the sum of lithostatic stress and tensile strength,

280   we assume that hydrofracturing occurs and increases permeability. Here, we consider

281   hydrofracturing of the aureole only, not within sill.

282   Second, we approximate the process of joint formation within the sill through a linear porosity-

283   permeability increase that is a function of temperature. Geological observations from the

284   Neuquén Basin suggest that an open (cooling) joint network developed in the sills through

285   which hydrocarbon-bearing hydrothermal fluids entered the sill while it was still hot enough to

286   cause graphitization (Figure 2, Figure 3, Figure 4). Cooling joints form as a result of bulk volume

287   reduction of the cooling and crystallizing magma, which induces thermal stresses that lead to

288   the formation of a cooling joint network, creating primary porosity and permeability inside the

289   intrusion (e.g., Petford, 2003; Hetényi et al., 2012). The overall pore-space gained in the model

290   is set to equate 8% volume loss, occurring during the transition from a melted to crystallized

291   magma (between the liquidus and solidus temperature), based on reported fracture porosities

292   from fractured sill reservoirs in the study area (Witte et al., 2012; Spacapan et al., 2020). To be

293 consistent with the crystal-mush model described by Marsh (2002), the onset of the pore

294 opening should be when 50-55% of the magma has crystallized. Here we take a value of

295 1000°C as the onset of the brittle-ductile-transition (BDT) temperature. Using a linearized,

296 temperature-dependent definition of the melt fraction, $(T-T_S)/(T_L-T_S)$, with T_L = 1100°C and

297 T_S = 900°C being liquidus and solidus temperatures, resp., the set value for the BDT in our

298 simulations implies that cooling joint creation starts when, at any distance from the sill margins,

299 50% of the sill has crystallized.

300 Note that in this way, we limit the model's representation of fracturing in the sill to cooling

301 joints and thus perform a strong simplification compared to the complex interplay of fracturing

302 mechanisms observed in the field (cf. section 3 and Rabbel et al, 2021). However, the goal is

303 to study the general impact of permeable sills on hydrothermal flow and the associated

304 hydrocarbon transport, which should be possible even with this limitation.

305

3.3 Modeling setup

307 We designed our modeling study to approximate the conditions of our study area, although

308 we simplified the setup for the sake of a well-constrained parameter study. Figure 5 and Table

309 1 show the model setup and the list of important model parameters, respectively.

310 The model domain extends from the surface to 500 m below the emplacement depth of the

311 sill. We assume instantaneous sill emplacement at 1100°C, corresponding to the inferred

312 liquidus temperatures of andesitic magma in the study area (Spacapan et al., 2018). Since

313 flow patterns around idealized flat sills tend to be symmetric, we limited our studies to a 500

314 m long "half", flat sill intrusion (Figure 5a). This allows to evaluate processes around and

315 within the sill at very high resolution of 0.5 m. The left and right boundaries are insulating

316 and impermeable, and we calibrated the temperature at the bottom boundary to create a

317 geothermal gradient of around 30°C/km. The top boundary mimics the behaviour of the sea

318 floor with free in- and outflow. Otherwise, initial conditions consider no basin history such as

319 uplift and erosion, and no pre-existing thermal maturation before sill emplacement. We

320 justify this by low background maturity values reported in the study area (Spacapan et al.,

321 2018; Palma et al., 2019; Rabbel et al., 2021)

322   For the sediments, we chose a homogenous material with 5% TOC and ca. 5 weight percent

323   bound water, as well as exponential decay of porosity with depth (Figure 5b). Permeability is

324   porosity-dependent and follows a Kozeny-Carman relationship. All values are calibrated to

325   local organic-rich shale, i.e. low porosity and low permeability rocks (Figure 5b). We chose

326   the specific values to match properties of Agrio and Vaca Muerta formations at 2-3 km depth
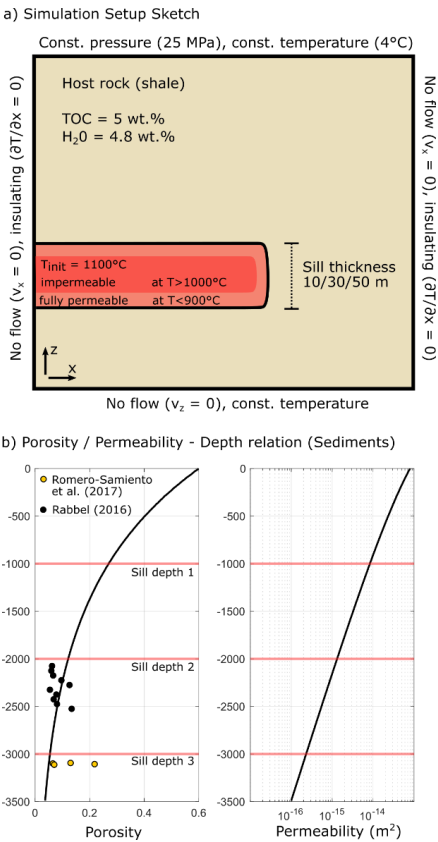
Figure 5. Illustration of the numerical modelling setup. (a) Sill geometry, boundary and initial conditions (not to scale). (b) Left: Porosity-depth relationship calibrated using reported data from the Vaca Muerta formation from various depths (Rabbel 2017, Romero-Samiento et al. 2017). Right: Permeability as a function of depth-

327

328   in the northern Neuquén Basin, which corresponds to emplacement depths for the igneous

329   petroleum systems present in both subsurface and outcrop.

330

331

332

333 **3.4 Parameter sensitivity study**

334 In total, we ran 27 simulations to investigate the effects of

335   o   porosity and permeability generation within sills

336   o   emplacement depth, i.e., sediment permeability and porosity (1, 2, 3 km)

337   o   intrusion thickness (10, 30, 50 m)

338 We first conduct a series of reference setups including permanently impermeable sills but

339 allowing hydraulic fracturing of the host rock. All combinations of emplacement depth and

340 sill thickness lead to a total set of 9 reference simulations. Subsequently, we use the same

341 setups but activate temperature-dependent porosity and permeability generation for the sills.

342 Table 1. Material properties used for hydrothermal simulations

Fixed rock parameters	Value	Unit
Fluid Properties	Follow eqn. of state for pure water (IAPS-84)	
Magma / Sill Properties (representing andesite)		
Specific heat capacity[1,2]	900	J kg^{-1} K^{-1}
Latent heat of crystallization[1,2]	320	kJ/kg
Initial sill temperature[3,4]	1100	°C
Liquidus temperature[3]	1100	°C
Solidus temperature[4]	900	°C
Brittle-Ductile-Transition (permeability creation)	1000-900	°C
Permeability range in sill[4]	10-20 – 10-15	m^2
Sill thickness[4]	10, 30, 50	m
Magma density[2,6]	2830	kg/m^3
Thermal conductivity	2.51	W m^{-1} K^{-1}
Host Rock Properties (representing shale)		
Density[6]	2600	kg/m^3
Specific heat capacity[5]	960	J kg^{-1} K^{-1}
Thermal conductivity[5]	2.55	W m^{-1} K^{-1}
Porosity[6]	Ref fig	Ref fig
Permeability	Ref fig	Ref fig
Initial TOC[4]	0.05	1
Initial bound water content[2]	0.048	1
Tensile strength[7]	3	MPa

Sources:

[1]Aarnes et al. (2010), [2]Galerne and Hasenclever (2019), [3]Stern et al. (1975) [4], Spacapan et al. (2018),
[5]Angenheister et al. (1982), [6]Rabbel (2017), [7]Schön (2015)

343

3.5   Numerical Simulation: results

345   3.5.1   Impermeable sill: Flow focusing and methane plume

346   We first present the results of the reference simulation of a 50 m thick, impermeable sill

347   emplaced at 3 km depth. Figure 6 displays the evolution of temperature, vitrinite reflectance

348   (Ro) as a proxy for thermal maturity, permeability and methane concentrations in the model

349   1, 64 and 1000 years after the sill is emplaced. In the first few years after emplacement (left

350   column in Figure 6), the sill is still over 1000°C hot and only the host rock very close to the sill

351   is heated to temperatures of >350°C. Within the thin, barely visible thermal aureole, thermal

352   maturity increases strongly and mineral dehydration takes place. In the dehydrated area,

353   permeability increases from initial values of around 10^{-16} to 10^{-15} m^2 (Figure 6g). Figure 6g also

354   shows a wider area of increased permeability indicated by the white dotted outline, which

355   corresponds to the extent of hydrofracturing. The organic matter in the shale close to the

356   contact shows a strong initial methane release, which travels toward the tip, where a small

357   initial methane plume rises above the intrusion (Figure 6j).

358   After 64 years (central column in Figure 6), the high-temperature aureole in the surrounding

359   host rock has expanded as the sill progressively cools down (Figure 6b). Within a distance of

360   about 50 m around the sill, thermal maturity has reached Ro values above 2, which indicates

361   the gas window or overmaturity (Figure 6e). Permeability in the same region is visibly

362   elevated because the clay minerals are partly or fully dehydrated (Figure 6h). However, no

363   more hydrofracturing occurs, since overpressures have dissipated and no longer exceed the

364   tensile failure criterion. Methane concentrations now show a wide plume of methane rising

365   on top of the sill and especially over its tip, but also a sizable accumulation remaining below

366   the sill (Figure 6k).

367   The right column in Figure 6 represents the end of the simulation after 1000 years. The

368   temperatures throughout the model are still elevated with respect to the initial geotherm but

369   are now below 200°C everywhere. The dehydration-related permeability increase has not

370   expanded significantly, but a second plume of very high methane concentrations is rising

371   above the sill, but at some distance to its tip. The peak of the first plume has reached ca. 300

m above the sill at this point. The aureole below the sill has also accumulated high methane
concentration of up to 800 kg per m^3 of water, which remain trapped below the impermeable
sill.
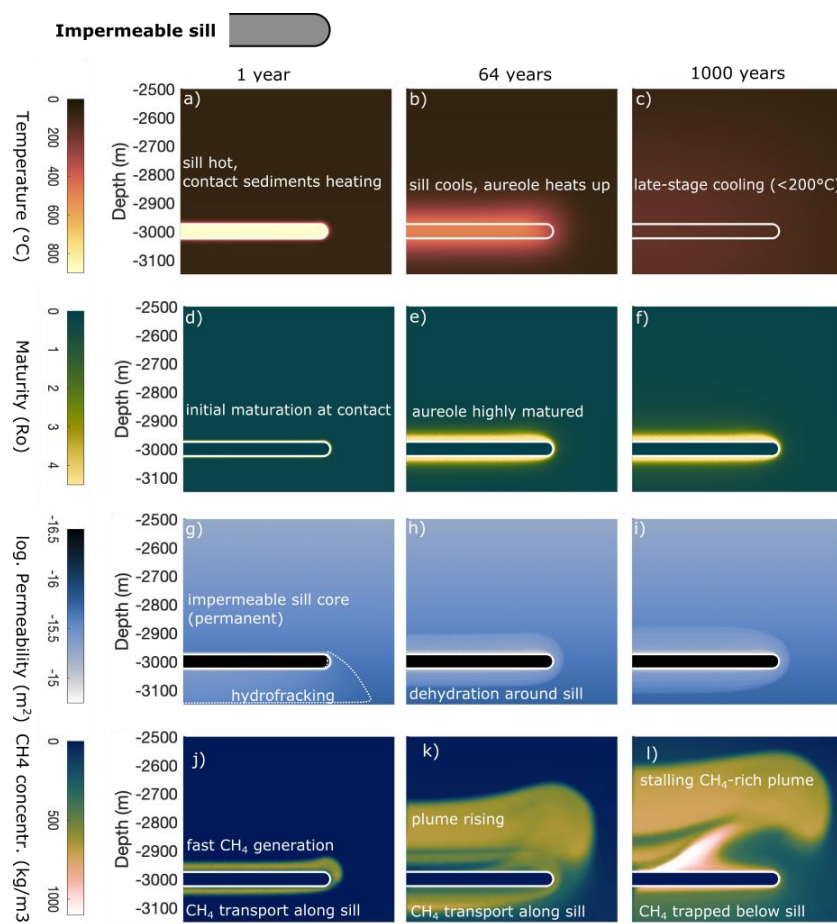
Figure 6. Reference simulation results for an impermeable sill of 50 m thickness at 3 km depth. The columns correspond to 1, 64 and 1000 years of simulated time after emplacement, respectively. The rows represent four parameters characterizing thermal state, contact metamorphism and hydrothermal transport of methane: (a-c) Temperature, (d-f) thermal maturity / organic matter transformation as vitrinite reflectance Ro, (g-i) permeability, (j-l) methane concentration.

3.5.2   Permeable sill: Pressure release and flow reversal

The introduction of cooling-related permeability generation in the sill profoundly changes the
development of hydrothermal flow and methane transport patterns. We show identical

379   parameters and time steps as for the reference simulations, i.e. temperature, vitrinite

380   reflectance (thermal maturity), permeability and methane concentrations in the model area

381   around the permeable sill (Figure 7). To describe the details of the evolving flow patterns, we

382   add close-up figures for methane concentration and flow velocities displaying flow vectors as

383   well as the accumulation of methane and average temperature in the permeable and porous

384   sill (Figure 8).

385   In the early phase, initial cooling of the sill leads to a progressing permeability front where

386   the temperatures approach the solidus defined as 900°C. At this stage, the simulation closely

387   resembles the reference run (Figure 7, left column). Temperatures in the sediments are

388   elevated only very close to the intrusion, where the sediments almost instantly produce gas or

389   become thermally overmature, i.e. vitrinite reflectance is larger than 1.5 (Figure 7a, d).

390   Permeability in the sediments increases due to dehydration near the intrusion contact and

391   hydrofracturing in the area within the dotted line below the sill (Figure 7g). Although large-

392   scale methane concentrations appear nearly identical to the reference scenario, the detailed

393   view shows that the onset of porosity and permeability generation in the sill's outermost

394   regions allows some limited methane transport into the sill (Figure 8a.1). Nevertheless, most

395   fluid flow and methane transport occur parallel to the sill contact and only rise upward

396   around the sill tip (Figure 8a.1, a.4). Since methane generation in the aureole continues but

397   transport is directed sideways within the host rock, the fraction of methane stored in the sill

398   itself reduces (Figure 8b).

399   However, after the entire sill has become fully permeable, the flow direction along the sill

400   center suddenly changes from horizontal, contact-parallel to near-vertical (Figure 7h, k, Figure

401   8a.2, a.5). The hydrothermal fluids transport the high methane concentrations from the lower

402   aureole directly through the sill and into the upper aureole (Figure 7h, Figure 8a.2). In the upper

403   aureole temperatures and thermal maturity are now higher than in the lower aureole (Figure 7b,

404   e). At the same time, the flow directions at the intrusion tip also change and a circular flow

405   pattern develops centered around a vortex located at the top of the intrusion tip (Figure 8a.2,

406   a.5). This vortex initiates a downward directed flow that transports some of the methane from

407   the flat rising plume above the sill back towards and into the sill tip (Figure 7k). During this

408   phase of "methane flushing", more methane enters the sill from below and through the tip

409   than is lost through the top contact, and thus both absolute and fractional methane stored in

410   the intrusion rises until ca. 90 years of simulation (Figure 8b). Interestingly, the average

411   temperature in the sill during this stage is still between 400-800°C (Figure 8b). The flow of

412   fluids through the sill also leads to an increased cooling rate from the moment when the sill

413   becomes fully permeable, as is indicated by the "kink" of the temperature curve at ca. 20

414   years (Figure 8b). Note also that the flow velocities drop by about 2 orders of magnitude

415   compared to the initial years and are now on the order of 10 cm/year after 64 years of

416   simulation.

417   In the following phase until the end of the simulation, the sill and sediments cool down to

418   below 200°C, and thermal maturity and permeability only increase marginally (Figure 7c, f, i).

419   The release of methane previously trapped under the sill creates a slowly rising band of very

420   high methane concentrations above the sill (Figure 7l). At the tip, continuous circular flow

421   creates a spatially confined area of very high methane concentration (Figure 8a.3, a.6).

422   However, flow velocities have further reduced by another 2 orders of magnitude (Figure 8a.6).

423   Overall, the sill maintains the total amount of stored methane due to approximately equal

424   inflow and outflow (Figure 8b). However, since methane generation continues in the shale, the

425   fraction of total methane stored in the sill reduces to ca. 5% from 500 years of simulation and

426   onwards.

427   In summary, we identify three hydrothermal flow phases in the case of a sill with

428   permeability evolution due to cooling joints. These include (i) pre-fracturing contact-parallel

429   flow and methane transport, (ii) post fracturing methane-flushing and partial backflow and

430   (iii) stabilization of methane in sill and late-stage methane generation.

431

432
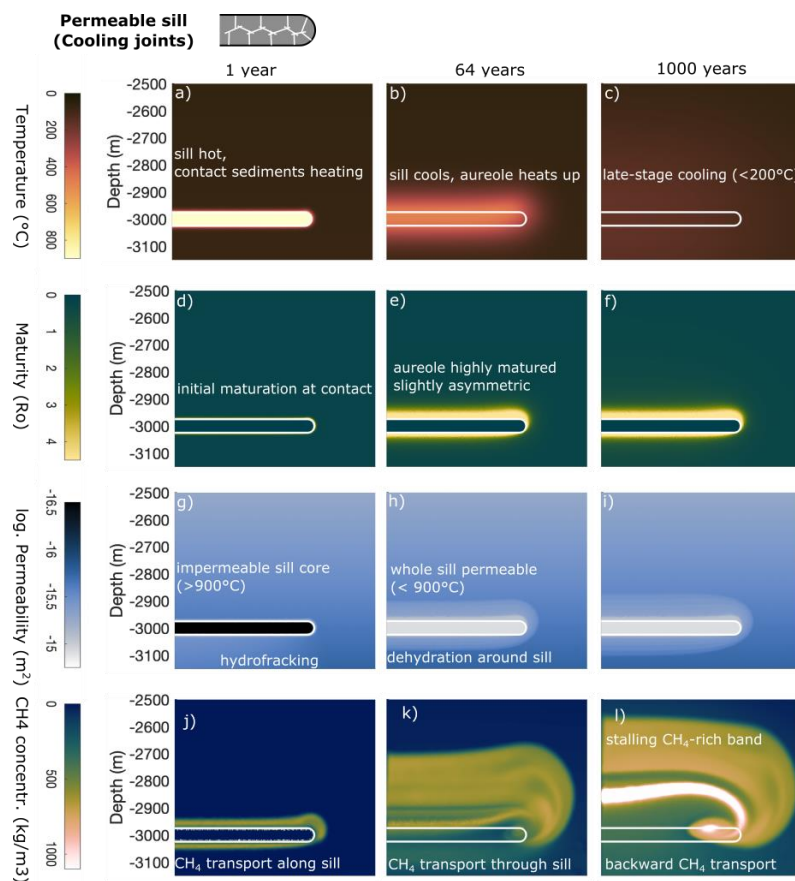
Figure 7. Simulation results for identical conditions as the reference case in Figure 6 (50 m thick, 3 km depth), but the sill develops porosity and permeability with cooling. The columns correspond to 1, 64 and 1000 years of simulated time after emplacement, respectively. The rows represent four parameters characterizing thermal state, contact metamorphism and hydrothermal transport of methane: (a-c) Temperature, (d-f) thermal maturity / organic matter transformation as vitrinite reflectance Ro, (g-i) permeability, (j-l) methane concentration.

433

434
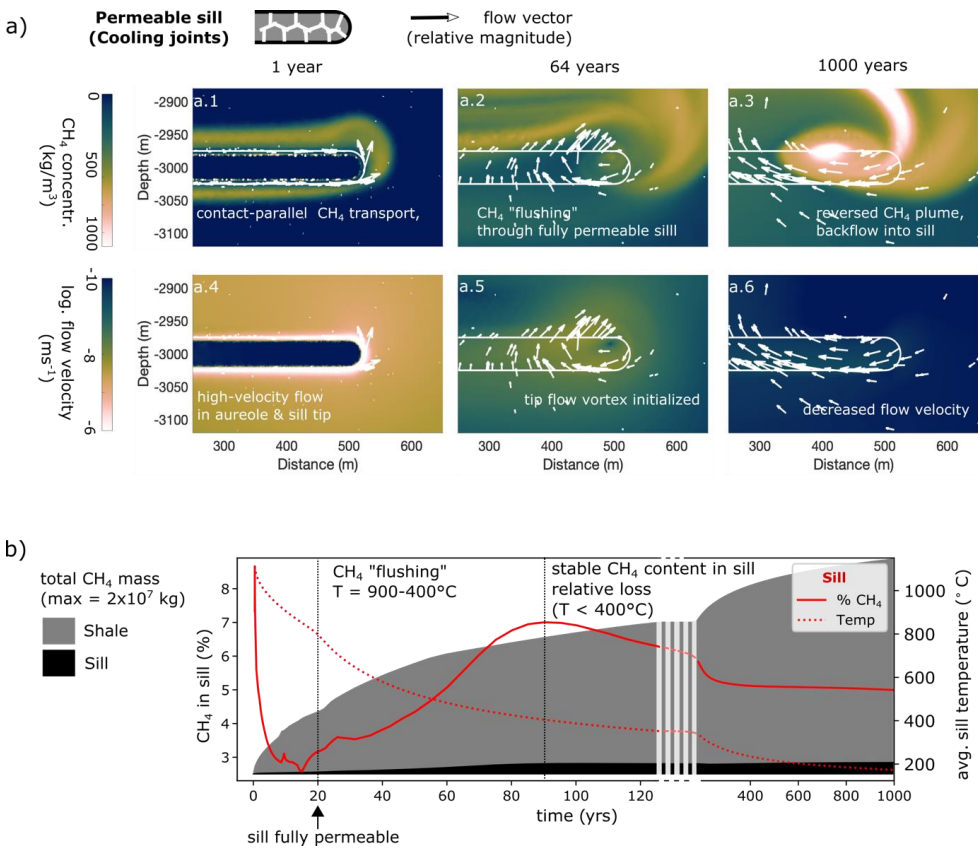
Figure 8. (a.1-a.6) Detailed view of the simulation of a permeable sill (50 m thick, 3 km depth, cf. Figure 7). The columns correspond to 1, 64 and 1000 years after emplacement, respectively. The rows show methane concentration (a.1-a.3) and flow velocity (a.4-a.6). The arrows represent flow vectors, with length differences representing relative magnitudes. Note that irregular arrow spacing is due to increased mesh fineness in and around the sill. (b) Fraction of total methane stored in the sill (solid line) and average temperature inside the sill (dotted line) throughout the simulation displayed above. Note that x-axis scaling is changed after 125 years, as indicated visually.

435

436

437

438

439

3.5.3 Effects of emplacement depth and sill thickness

Finally, we explore the influence of emplacement depth and sill thickness on the resulting hydrothermal flow and methane transport pattern in case of a permeable sill (Figure 9). Not surprisingly, deeper and larger sills lead to more methane generation, but the transport of methane differs significantly because the flow patterns are affected in several ways. First, backward flow toward the intrusions similar to that described in the former section occurs only for deep emplacement depths, i.e. generally low permeability of the host rock due to burial, and for relatively thick intrusions (Figure 9a, d, g). In contrast, very thin intrusions (10 m) mainly generate a thick band of rising methane but little to no backflows at this depth (Figure 9f, i).
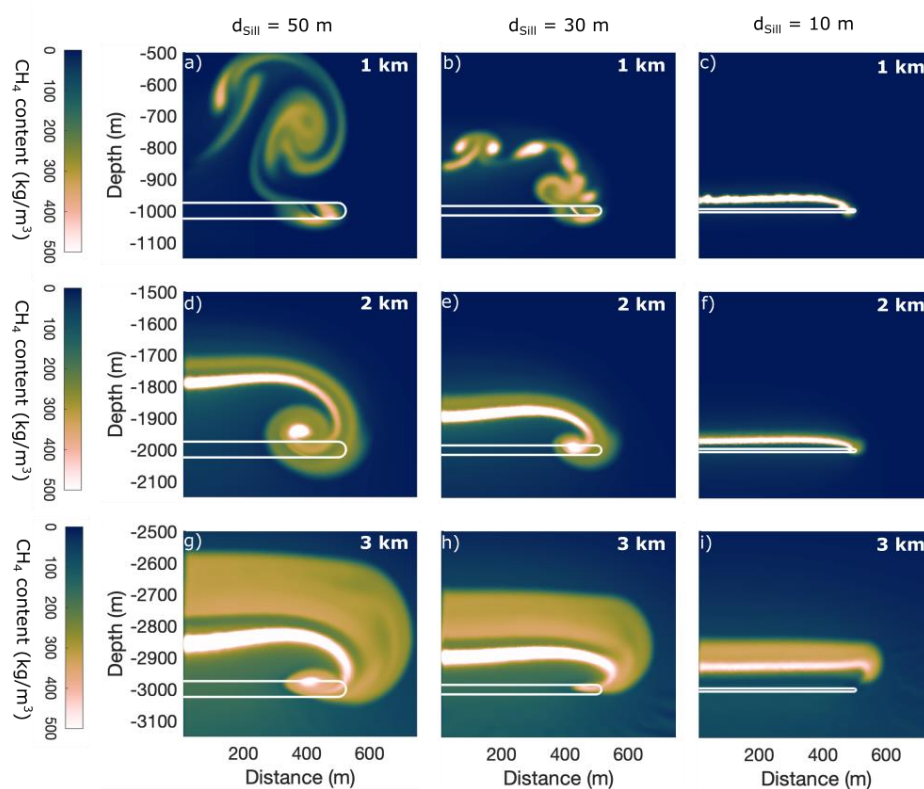
Figure 9. Parameter study results for the effect of varying emplacement depths and sill thicknesses on the final methane distribution after 1000 years, assuming a permeable sill. The columns represent different thicknesses of 50 m, 30 m and 10 m, respectively. The rows show emplacement depths of 1 km, 2 km, and 3 km, respectively, and thus include associated changes in host rock porosity and permeability as displayed in Figure 2b.

450 At 1km depth, however, the characteristics of the hydrothermal flow patterns change

451 drastically. Although some methane remains inside and below the sill tip, the backflow

452 around a tip-vortex is no longer the dominant feature. Instead, hydrothermal convection cells

453 develop above the intrusion and a methane plume rises towards the surface (Figure 9a,b). After

454 1000 years, the plume generated by the 50 m thick sill has risen by 500m, which is more than

455 double compared to the 30 m thick sill at the same depth, or a 50 m thick sill at 2 km depth

456 (Figure 9a, b, d).

457

458 4   Interpretation and discussion

459 4.1   Hydrocarbon transport through hot sills

460 Outcrop data strongly suggests that transport of hydrocarbons generated around the sills in

461 the northern Neuquén Basin occurs both vertically through the igneous intrusions as well as

462 around their tip. Importantly, geochemical data from the study area suggests that the sills are

463 responsible for most, if not all, organic matter transformation in the host rock, because

464 background maturity between the sills is essentially zero (Spacapan et al., 2018; Rabbel et al.,

465 2021). We thus interpret the observed hydrocarbons in the field to result from magmatic and

466 hydrothermal activity rather than burial-related maturation.

467 Cooling joints and veins or dykes filled with black shale and bitumen are pervasive

468 throughout the fracture networks of sills in our study area (Figure 2 and Figure 3). The example

469 shown in Figure 2 is particularly clear in showing the relationship between upwelling fluidized

470 structures and the fill of the cooling joints. Note that similar observations have been

471 documented in other outcrops at larger scales (Rabbel et al., 2021). We therefore propose that

472 the flow of hot fluids and fluidized sediments through sills is a common occurrence in the

473 northern Neuquén Basin. We thus provide solid outcrop evidence that sills can become a

474 preferred hydrocarbon transport pathways upon cooling. In contrast, this finding contradicts

475 the widespread assumption of impermeable intrusions in modeling studies of hydrothermal

476 fluid flow in volcanic basins (e.g., Iyer et al., 2013; Iyer et al., 2017; Galerne and

477 Hasenclever, 2019).

478 Our observations complement numerous growing evidence of hydrocarbons or fluidized

479 sediments within sills of widely different sizes exist for instance in the Faroe-Shetland Basin

480 (Rateau et al., 2013; Schofield et al., 2020), Karoo Basin (Svensen et al., 2010) and Guyamas

481   Basin (Teske et al., 2021). Svensen et al. (2010) found metamorphosed sandstone dykes

482   within dolerite sills in the Karoo Basin with mineral assemblage indicative of temperatures

483   >300°C. They proposed that strong pressure gradients between the overpressured host rocks

484   and the solidifying and contracting sill intrusions are likely responsible for liquefied

485   sediments entering the intrusions shortly after cooling. Similar to this study, Svensen et al.

486   (2010) based this interpretation on coupled thermo-hydraulic models, but explicitly

487   considered thermal contraction of the magma. Although our approach of adding porosity to

488   the sill is a simplification of this process, the general mechanism of hydrocarbon-rich fluids

489   and sediments entering the cooling joint network in the intrusions in the Neuquén Basin is

490   similar. We thus infer that our observations of hydrocarbon flow through hot sills in the

491   Neuquén Basin are widespread in volcanic basins worldwide.

492

493   **4.2   Impact of permeable sills on hydrothermal flow**

494   Our numerical simulations allow us to assess the effects of implementing porosity and

495   permeability increase due to fracturing when the sill has reached the solidus temperature. In

496   simulations with an impermeable (i.e., unfractured) sill, the intrusion acts as a constant

497   barrier for the hydrothermal flow and methane transport, and only the aureole shows

498   permeability evolution due to fracturing and dehydration (Figure 6a, d, g). In this

499   configuration, a upward-rising methane plume initiates from the top contact of the sill. In

500   addition, large amounts of methane are trapped below the sill, since no vertical pathways are

501   available through the sill (Figure 6g, j).

502   In contrast, a permeable sill introduces drastic changes in the flow and methane transport

503   patterns, and results in three distinct phases with very different characteristics.

504   *Phase 1: Impermeable sill and contact-parallel flow.* Prior to complete solidification, the sill

505   acts as a flow boundary and the flow patterns are essentially the same as in the reference

506   simulation, i.e., rising methane above the sill and contact-parallel flow and extensive

507   hydrofracturing below the sill (Figure 6g, j; Figure 7g, j, Figure 8a.1, a.4). Hydraulic fractures in

508   the aureole and around the sill edge initiate in this early phase, which may lead to the

509   formation of the large bitumen dykes and calcite veins observed in the field (Figure 3).

510   *Phase 2: Hydrothermal "flushing" through solidified, permeable sill.* The generation of

511   cooling-related porosity and permeability inside the sill initiates the abrupt change from

512   contact-parallel flow towards the intrusion tip to vertical uprising through the sill (second

513   column of Figure 7, Figure 8a.2, a.5). This effect is responsible for a rush of hydrocarbon (here:

514   methane) -rich fluids through the sill at average temperatures of 400-800°C (Figure 8b),

515   because the large overpressure below the sills can now drive fluid flow straight upwards and

516   dissipate instead of supplying a steady flow toward the sill tip. In addition, porosity

517   generation inside the sill creates a suction effect that drives fluids into the intrusion (cf.

518   Svensen et al., 2010). Considering flow velocities after 64 years (Figure 8a.2, a.5), the model

519   shows that fluids flowing through a 50 m thick sill are exposed to this environment for tens of

520   years, which could be sufficient for graphite generation and therefore seems to fit well with

521   outcrop data and models for hydrothermal graphite generation (Figure 4; Rumble, 2014).

522   *Phase 3: Vortex phase and reversed flow.* The sudden change in the pore pressure

523   distribution due to permeability creation within the sill also initiates the vortex observed

524   above the sill tip and leads to the observed flow reversal and methane transport towards the

525   sill tip (right column Figure 7; Figure 8a.3, a.6). However, in the long run the amount of

526   methane influx toward the sill approximately equals the loss through upward flow so that the

527   amount of methane is stable within the sill, and the fraction of total methane stored in the sill

528   reduces after the "flushing" phase (Figure 8b). Hydrocarbons entering the sill in this last phase

529   does not experience the extreme temperatures and have better chances of survival.

530   4.3   Impact of depth and thickness of permeable sills on hydrothermal flow

531   The first two phases, i.e. contact-parallel flow followed by methane "flushing", occur in all

532   simulations with permeability creation within the cooling sill in a very similar fashion, which

533   fits well with the fact that we observe graphitic material in sills of all sizes in the field.

534   However, the final flow configuration and methane distribution shows important differences

535   with intrusion thickness and emplacement depth (Figure 9). At depths of at least 2 km, i.e.,

536   emplacement depths approximately corresponding to the Agrio and Vaca Muerta formations

537   in the study area, the dominant feature is the backflow at the sill tip from an otherwise evenly

538   rising band of very high methane concentration (Figure 9d, g). Conversely, for the shallowest

539   case (1 km), higher background permeability now allows the formation of large convection

540   cells that transport methane towards the surface, while accumulation in the sill itself is very

541   limited (Figure 9a). Thus, shallow permeable sills seem to favour hydrothermal upward

542   transport of methane. This conclusion corresponds well with the results of Iyer et al. (2013)

543   who found that in shallow, high permeability settings, release of fluids through permeable

544   sills could be an important factor for greenhouse gas emissions from contact aureoles of sill

545   intrusions.

546   Furthermore, the thinnest sills modelled do not have sufficient thermal energy to create the

547   required pressure anomaly to sustain a flow vortex and backward flow of methane similar to

548   the larger intrusions (Figure 9c, f, i). This is especially true for the deeper intrusions, where

549   lower permeability of the host rock generally inhibits fluid flow. Since most of the sills

550   emplaced in our study area are less than 30 m thick, we expect that only few sills create

551   significant backflow.

4.4   Implications for fluid flow and methane transport

553   The strong contrast between the simulations with permeable and impermeable sills has

554   important implications for the understanding of hydrothermal flow in volcanic basins, and

555   notably on the formation of hydrothermal vent complexes and gas release to the atmosphere.

556   Permeable sills strongly favor upward vertical flow and fluid pressure dissipation, especially

557   in low-permeability host rocks, whereas impermeable sills favor fluid pressure build-up and

558   contact-parallel flow towards sill tips. These latter mechanisms are the main responsible for

559   the formation of hydrothermal vent complexes at sill tips (Iyer et al., 2017; Galerne and

560   Hasenclever, 2019). Conversely, since the opening of vertical pathways through the sills due

561   to cooling joints efficiently dissipates overpressure, permeable sills could potentially inhibit

562   vent formation, or at least reduce atmospheric degassing.

563   Although we do not attempt to model vent formation here, our study can serve as a starting

564   point to investigate the favorable conditions for hydrothermal vent formation. Our findings

565   suggest that imposing impermeable sills in hydrothermal models is a strong assumption that

566   may artificially ease the formation of hydrothermal vent complexes. Although there are good

567   arguments to assume that massive, unfractured and impermeable intrusions dominate in many

568   volcanic basins, the growing evidence of permeable sills during cooling (see section 6.1)

569   suggests that this assumption should be critically evaluated on a case-by-case basis, and

570   might explain the lack of hydrothermal vent complexes in some volcanic basins, like in the

571   Neuquén Basin. We argue that future hydrothermal modelling studies of intrusion in

572   sedimentary basins need to include sound justification for the chosen permeability and

573   porosity evolution of the sills.

574   Additionally, the occurrence of graphitic bitumen in dykes and as filling of cooling joints

575   indicates that part of the carbon gases rising through permeable sills could be reduced to

576   graphite and be stored as solids (Figure 2, Figure 3, Figure 4). This fraction of carbon is

577   strapped permanently underground and is not available for degassing in the atmosphere. The

578   widespread observations of graphite in the field suggests that a significant fraction of

579   hydrocarbons matured in the sills metamorphic aureoles may not be mobilized. Currently,

580   the fraction of methane transformed to immobile graphite, and so how much this reduced

581   methane transport, is not known.

582

4.5   Implications for igneous petroleum systems in the Río Grande Valley

584   Our study also provides further insight into the evolution of the igneous petroleum systems in

585   the Río Grande Valley, in particular with respect to the timing of the charging of the igneous

586   hydrocarbon reservoirs. The current conceptual models comprise three main phases after sill

587   emplacement into the previously immature shale formations (Witte et al., 2012; Spacapan et

588   al., 2018; Spacapan et al., 2020). During the initial "thermal stage", the heat input from the

589   sills generates liquid and gaseous hydrocarbons. During the second so-called "cooling stage",

590   hydrocarbons hydrothermally migrate into the sill once cooling joints form. The last stage

591   comprises tectonic fracturing and late-stage migration of hydrocarbons into the sills.

592   In this model, a significant part of the producible hydrocarbons migrates into the sill during

593   the cooling stage, after the formation of colling joints. However, our study shows that

594   hydrocarbons indeed migrate into the intrusions when the cooling joint network has formed,

595   but experience far too high temperatures (at least 400°C) for them to survive as producible

596   liquids or gases. In addition, regardless the scenarios tested in our simulations, temperatures

597   during the main phase of accumulation of hydrocarbons in the intrusion still exceed 300°C

598   (Figure 8b). Therefore, a survival of hydrocarbons entering the cooling joint network shortly

599   after its creation seems highly unlikely. This result suggests that the charging of the igneous

600   reservoirs occurs during the late-stage cooling of the sills, and after significant amounts of

601   hydrocarbons has flowed through the sills at high temperature. The cooling stage of the

602   models proposed earlier thus needs to be revised and split into two sub-stages: (1) a first

603   influx of hydrocarbons through still hot sills, with no survival hydrocarbons, and (2) a later

604   migration of hydrocarbons within the cooled sill, where the hydrocarbons can survive and be

605   trapped to form producible reservoirs.

606

4.6   Study limitations and future recommendations

607   Finally, we present selected recommendations for future work arising from the limitations of
608   our study. Despite the complexity of the current numerical model, some known processes are
609   not yet considered. First, mineral precipitation at high temperatures can occur at non-
610   negligible rates and lead to fast porosity-decrease, causing pore pressure increase and
611   possibly fracturing (Townsend, 2018). Fracturing in the aureole may not be reversible but
612   permanently increase porosity and permeability, which has been documented in systematic
613   core studies of contact aureoles in the RGV (Spacapan et al., 2019). These features should be
614   included in future research, and the model predictions tested against field and laboratory
615   studies. Finally, due to the strong effect on hydrothermal flow, it is critical to investigate
616   under which circumstances cooling joints, which exist in many sheet intrusions, become
617   available flow pathways.

618

619   # 5   Conclusions

620   In this study, we integrate geological field data with numerical models to investigate
621   hydrothermal transport of hydrocarbon-rich fluids around fractured igneous sills. We use
622   outcrops of fractured sills emplaced in organic-rich shales in the northern Neuquén Basin to
623   establish that sills can become permeable fluid pathways upon solidification, which affects
624   the fate of locally generated hydrocarbons. The numerical modelling study allows us to
625   understand the main phases of hydrothermal flow and the kilometre-scale flow patterns in
626   response to porosity and permeability generation inside a sill intrusion. This provides new
627   insights into hydrothermal flow in volcanic sedimentary basins, because previous studies
628   commonly assume that sills represent permanently impermeable bodies. The main
629   conclusions of this study are as follows:

630   1. Widespread occurrence of veins with solid, strongly graphitized bitumen as well as
631   cooling joints filled with solid bitumen or organic-rich shales evidence transport of
632   hydrocarbon-rich fluids and liquefied sediments into the sill in a high-temperature
633   (probably >350°C), high-pressure environment.

634

2. Numerical modelling indicates three distinct flow phases around sills that become porous and permeable upon solidification, which affects transport of hydrocarbons generated in the contact aureole:

   (1) Contact-parallel flow toward the tip prior to solidification, creating an early plume above the sill tip

   (2) Sudden change to vertical flow upon complete solidification and "flushing" of hydrocarbons from the lower contact aureole upwards through the sill. This almost instantly dissipates much of the overpressure below the sill.

   (3) "Post-flushing" flow regime with slow rise of hydrocarbon-rich fluids above the sill center, and backward-downward flow towards the sill tip due to a vortex initialized by the sudden pressure reconfiguration

3. Simulations indicate that "flushing" of methane through the sill occurs at temperatures >400°C, which meets the conditions for hydrothermal graphitization. This may explain field observations of graphitic bitumen dykes.

4. Migration via reverse flow through a tip vortex during the post-flushing phase is very limited or absent for thin sills (< 30m) in low-permeable host rocks, which applies to many sill in the study area.

5. Permeability creation with the cooling sills may considerably reduce pressure build-up below the sills, and thus reduce the potential for hydrothermal venting. With growing evidence for permeable sills in volcanic basins globally, the permeability evolution of sills should be addressed in future modelling studies focused on sill-related venting.

6. In contrast to proposed conceptual models, flow of hydrocarbons into newly formed cooling joints is likely not a viable migration mechanism for igneous sill reservoirs in the northern Neuquén Basin, as the intrusions are too hot for survival of liquid hydrocarbons.

665   **Acknowledgements**

666   Rabbel's position was funded by the Faculty of Mathematics and Natural Science of the

667   University of Oslo, through the "Earth Flows" Strategic Initiative project. The DEEP

668   Research School provided funding for fieldwork (249040/F60).

669

670

671   **References**

672   Aarnes, I., Podladchikov, Y.Y., Svensen, H., 2012. Devolatilization-induced pressure build-up:

673   Implications for reaction front movement and breccia pipe formation. Geofluids 12, 265-279,

674   10.1111/j.1468-8123.2012.00368.x.

675   Aarnes, I., Svensen, H., Connolly, J.A.D., Podladchikov, Y.Y., 2010. How contact metamorphism can

676   trigger global climate changes: Modeling gas generation around igneous sills in sedimentary

677   basins. Geochimica et Cosmochimica Acta 74, 7179-7195,

678   http://dx.doi.org/10.1016/j.gca.2010.09.011.

679   Angenheister, G., Cermak, V., Huckenholz, H., Rybach, L., Schmid, R., Schopper, J., Schuch, M.,

680   Stoeffler, D., Wohlenberg, J., 1982. Physical properties of rocks. Subvol. a.

681   Beyssac, O., Goffé, B., Chopin, C., Rouzaud, J.N., 2002. Raman spectra of carbonaceous material in

682   metasediments: a new geothermometer. Journal of Metamorphic Geology 20, 859-871,

683   10.1046/j.1525-1314.2002.00408.x.

684   Buseck, P.R., Beyssac, O., 2014. From organic matter to graphite: Graphitization. Elements 10, 421-

685   426.

686   Chevallier, L., Gibson, L.A., HNhleko, L.O., Woodford, A.C., Nomquphu, W., Kippie, I., 2004.

687   Hydrogeology of fractured-rock aquifers and related ecosystems within the Qoqodala dolerite

688   ring and sill complex, Great Kei catchment, Eastern Cape, Water Res. Com., S. Afr., p. 127.

689   Cobbold, P.R., Diraison, M., Rossello, E.A., 1999. Bitumen veins and Eocene transpression, Neuquén

690   basin, Argentina. Tectonophysics 314, 423-442.

691   Combina, A., Nullo, F., 2005. Tertiary volcanism and sedimentation in the southern Cordillera

692   Principal, Mendoza, Argentina, in: Proceedings of the 6th International Symposium on

693   Andean Geodynamics, Barcelona, Spain, 12-14 September 2005, 174-177.

694   Connolly, J., 2009. The geodynamic equation of state: what and how. Geochemistry, Geophysics,

695   Geosystems 10.

696   Delaney, P.T., 1982. Rapid intrusion of magma into wet rock: Groundwater flow due to pore pressure

697   increases. Journal of Geophysical Research: Solid Earth 87, 7739-7756.

698 Einsele, G., Gieskes, J.M., Curray, J., Moore, D.M., Aguayo, E., Aubry, M.-P., Fornari, D., Guerrero,
699   J., Kastner, M., Kelts, K., Lyle, M., Matoba, Y., Molina-Cruz, A., Niemitz, J., Rueda, J.,
700   Saunders, A., Schrader, H., Simoneit, B., Vacquier, V., 1980. Intrusion of basaltic sills into
701   highly porous sediments, and resulting hydrothermal activity. Nature 283, 441-445, doi:
702   10.1038/283441a0.

703 Galerne, C.Y., Hasenclever, J., 2019. Distinct Degassing Pulses During Magma Invasion in the
704   Stratified Karoo Basin—New Insights From Hydrothermal Fluid Flow Modeling.
705   Geochemistry, Geophysics, Geosystems 20, 2955-2984, 10.1029/2018GC008120.

706 Hays, W.W., Nuttli, O.W., Scharon, L., 1967. Mapping gilsonite veins with the electrical resistivity
707   method. Geophysics 32, 302-310.

708 Hetényi, G., Taisne, B., Garel, F., Médard, É., Bosshard, S., Mattsson, H.B., 2012. Scales of columnar
709   jointing in igneous rocks: field measurements and controlling factors. Bulletin of
710   Volcanology 74, 457-482, 10.1007/s00445-011-0534-4.

711 Howell, J.A., Schwarz, E., Spalletti, L.A., Veiga, G.D., 2005. The Neuquén Basin: an overview, in:
712   Veiga, G.D., Spalletti, L.A., Howell, J.A., Schwarz, E. (Eds.), Geological Society, London,
713   Special Publications, 252, 1-14.

714 Iyer, K., Rüpke, L., Galerne, C.Y., 2013. Modeling fluid flow in sedimentary basins with sill
715   intrusions: Implications for hydrothermal venting and climate change. Geochemistry,
716   Geophysics, Geosystems 14, 5244-5262, 10.1002/2013GC005012.

717 Iyer, K., Schmid, D.W., Planke, S., Millett, J., 2017. Modelling hydrothermal venting in volcanic
718   sedimentary basins: Impact on hydrocarbon maturation and paleoclimate. Earth Planet. Sci.
719   Lett. 467, 30-42, https://doi.org/10.1016/j.epsl.2017.03.023.

720 Jamtveit, B., Svensen, H., Podladchikov, Y.Y., Planke, S., 2004. Hydrothermal vent complexes
721   associated with sill intrusions in sedimentary basins. Physical Geology of High-Level
722   Magmatic Systems. Geological Society, London, Special Publications 234, 233-241.

723 Kay, S.M., Burns, W.M., Copeland, P., Mancilla, O., 2006. Upper Cretaceous to Holocene
724   magmatism and evidence for transient Miocene shallowing of the Andean subduction zone
725   under the northern Neuquén Basin. Geological Society of America Special Papers 407, 19-60.

726 Kietzmann, D.A., Palma, R.M., Riccardi, A.C., Martín-Chivelet, J., López-Gómez, J., 2014.
727   Sedimentology and sequence stratigraphy of a Tithonian–Valanginian carbonate ramp (Vaca
728   Muerta Formation): a misunderstood exceptional source rock in the Southern Mendoza area
729   of the Neuquén Basin, Argentina. Sedimentary geology 302, 64-86.

730 Kobchenko, M., Hafver, A., Jettestuen, E., Renard, F., Galland, O., Jamtveit, B., Meakin, P.,
731   Dysthe, D. K., 2014. Evolution of a fracture network in an elastic medium with
732   internal fluid generation and expulsion. Physical Review E, 90(5), 052801.

733   Kwiecinska, B., Suárez-Ruiz, I., Paluszkiewicz, C., Rodriques, S., 2010. Raman spectroscopy of
734   selected carbonaceous samples. International Journal of Coal Geology 84, 206-212.

735   Manceda, R., Figueroa, D., 1995. Inversion of the Mesozoic Neuquén rift in the Malargüe fold and
736   thrust belt, Mendoza, Argentina, in: Tankard, A.J., S., S., Welsink, H.J. (Eds.), Petroleum
737   basins of South America: AAPG Memoir, 62, 369–382.

738   Mark, N., Schofield, N., Pugliese, S., Watson, D., Holford, S., Muirhead, D., Brown, R., Healy, D.,
739   2018. Igneous intrusions in the Faroe Shetland basin and their implications for hydrocarbon
740   exploration; new insights from well and seismic data. Marine and Petroleum Geology 92,
741   733-753.

742   Marsh, B.D., 2002. On bimodal differentiation by solidification front instability in basaltic magmas,
743   part 1: basic mechanics. Geochimica et Cosmochimica Acta 66, 2211-2229,
744   https://doi.org/10.1016/S0016-7037(02)00905-5.

745   Nermoen, A., Galland, O., Jettestuen, E., Fristad, K., Podladchikov, Y.Y., Svensen, H., Malthe-
746   Sørenssen, A., 2010. Experimental and analytic modeling of piercement structures. J.
747   Geophys. Res. 115, B10202, 10.1029/2010jb007583.

748   Palma, J.O., Spacapan, J.B., Rabbel, O., Galland, O., Ruiz, R., Leanza, H.A., 2019. The atypical
749   igneous Petroleum System of the Cara Cura range, southern Mendoza province, Argentina, in:
750   The Physical Geology of Subvolcanic Systems: Laccoliths, Sills and Dykes (LASI6),
751   Malargüe, Germany, 25-29 November 2019, 159-161, 2019

752   Panahi, H., Kobchenko, M., Meakin, P., Dysthe, D.K., Renard, F., 2018. In-situ imaging of fracture
753   development during maturation of an organic-rich shale: Effects of heating rate and
754   confinement. Marine and Petroleum Geology 95, 314-327.

755   Petford, N., 2003. Controls on primary porosity and permeability development in igneous rocks.
756   Hydrocarbons in Crystalline Rocks 214, 93-107.

757   Potgieter-Vermaak, S., Maledi, N., Wagner, N., Van Heerden, J., Van Grieken, R., Potgieter, J., 2011.
758   Raman spectroscopy for the analysis of coal: a review. Journal of Raman Spectroscopy 42,
759   123-129.

760   Rabbel, O., 2017. Integrated Seismic and Rock Physics Modelling of Oil-Producing Volcanic Sills in
761   the Neuquén Basin, Argentina, Department of Geosciences. University of Oslo, Oslo, p. 83.

762   Rabbel, O., Galland, O., Mair, K., Lecomte, I., Senger, K., Spacapan, J.B., Manceda, R., 2018. From
763   field analogues to realistic seismic modelling: a case study of an oil-producing andesitic sill
764   complex in the Neuquén Basin, Argentina. J. Geol. Soc., 10.1144/jgs2017-116.

765   Rabbel, O., Mair, K., Galland, O., Grühser, C., Meier, T., 2020. Numerical modeling of fracture
766   network evolution in organic-rich shale with rapid internal fluid generation. Journal of
767   Geophysical Research: Solid Earth 125, e2020JB019445.

768 Rabbel, O., Palma, J.O., Mair, K., Galland, O., Spacapan, J.B., Senger, K., 2021. Fracture networks in
769   shale-hosted igneous intrusions: Processes, distribution and implications for igneous
770   petroleum systems. J. Struct. Geol. 150, 104403, https://doi.org/10.1016/j.jsg.2021.104403.
771 Rantitsch, G., Lämmerer, W., Fisslthaler, E., Mitsche, S., Kaltenböck, H., 2016. On the discrimination
772   of semi-graphite and graphite by Raman spectroscopy. International Journal of Coal Geology
773   159, 48-56.
774 Rateau, R., Schofield, N., Smith, M., 2013. The potential role of igneous intrusions on hydrocarbon
775   migration, West of Shetland. Petroleum Geoscience 19, 259-272, doi: 10.1144/petgeo2012-
776   035.
777 Rodriguez Monreal, F., Villar, H.J., Baudino, R., Delpino, D., Zencich, S., 2009. Modeling an
778   atypical petroleum system: A case study of hydrocarbon generation, migration and
779   accumulation related to igneous intrusions in the Neuquen Basin, Argentina. Marine and
780   Petroleum Geology 26, 590-605, doi: 10.1016/j.marpetgeo.2009.01.005.
781 Rumble, D., 2014. Hydrothermal graphitic carbon. Elements 10, 427-433.
782 Schiuma, M.F. Intrusivos del valle del Río Grande, provincia de Mendoza, su importancia como
783   productores de hidrocarburos, Ph.D. thesis, Universidad Nacional de La Plata, Argentina, 234
784   pp., 1994
785 Schofield, N., Holford, S., Edwards, A., Mark, N., Pugliese, S., 2020. Overpressure transmission
786   through interconnected igneous intrusions. AAPG Bulletin 104, 285-303.
787 Schön, J.H., 2015. Physical properties of rocks: Fundamentals and principles of petrophysics.
788   Elsevier.
789 Senger, K., Millett, J., Planke, S., Ogata, K., Eide, C., Festøy, M., Galland, O., Jerram, D.A., 2017.
790   Effects of igneous intrusions on the petroleum system: a review. First Break 35.6, 47-56,
791   10.3997/1365-2397.2017011.
792 Spacapan, J.B., D'Odorico, A., Palma, O., Galland, O., Rojas Vera, E., Ruiz, R., Leanza, H.A.,
793   Medialdea, A., Manceda, R., 2020. Igneous petroleum systems in the Malargüe fold and
794   thrust belt, Río Grande Valley area, Neuquén Basin, Argentina. Marine and Petroleum
795   Geology 111, 309-331, https://doi.org/10.1016/j.marpetgeo.2019.08.038.
796 Spacapan, J.B., D´Odorico, A., Palma, O., Galland, O., Senger, K., Ruiz, R., Manceda, R., Leanza,
797   H.A., 2019. Low resistivity zones at contacts of igneous intrusions emplaced in organic-rich
798   formations and their implications on fluid flow and petroleum systems: A case study in the
799   northern Neuquén Basin, Argentina. Basin Research, 10.1111/bre.12363.
800 Spacapan, J.B., Galland, O., Leanza, H.A., Planke, S., 2017. Igneous sill and finger emplacement
801   mechanism in shale-dominated formations: a field study at Cuesta del Chihuido, Neuquén
802   Basin, Argentina. J. Geol. Soc. 174, 422-433, 10.1144/jgs2016-056.
803 Spacapan, J.B., Palma, O., Galland, O., Manceda, R., Rocha, E., D'Odorico, A., Leanza, H.A., 2018.
804   Thermal impact of igneous sill complexes on organic-rich formations and the generation of a

805   petroleum system: case study in the Neuquén Basin, Argentina. Mar. Pet. Geol. 91, 519-531,

806   https://doi.org/10.1016/j.marpetgeo.2018.01.018.

807 Stern, C.R., Huang, W.-L., Wyllie, P.J., 1975. Basalt-andesite-rhyolite-H2O: Crystallization intervals

808   with excess H2O and H2O-undersaturated liquidus surfaces to 35 kolbras, with implications

809   for magma genesis. Earth and Planetary Science Letters 28, 189-196.

810 Svensen, H., Aarnes, I., Podladchikov, Y.Y., Jettestuen, E., Harstad, C.H., Planke, S., 2010.

811   Sandstone dikes in dolerite sills: Evidence for high-pressure gradients and sediment

812   mobilization during solidification of magmatic sheet intrusions in sedimentary basins.

813   Geosphere 6, 211-224.

814 Svensen, H., Planke, S., Malthe-Sørenssen, A., Jamtveit, B., Myklebust, R., Rasmussen Eidem, T.,

815   Rey, S.S., 2004. Release of methane from a volcanic basin as a mechanism for initial Eocene

816   global warming. Nature 429, 542-545, doi: 10.1038/nature02566.

817 Sweeney, J.J., Burnham, A.K., 1990. Evaluation of a simple model of vitrinite reflectance based on

818   chemical kinetics. AAPG bulletin 74, 1559-1570.

819 Teske A, Lizarralde D, Höfig TW, and the Expedition 385 Scientists (2021): Expedition 385

820   Summary. Proceedings of the International Ocean Discovery Program 385. doi:

821   10.14379/iodp.proc.385.101.2021

822 Townsend, M.R., 2018. Modeling Thermal Pressurization Around Shallow Dikes Using Temperature-

823   Dependent Hydraulic Properties: Implications for Deformation Around Intrusions. Journal of

824   Geophysical Research: Solid Earth 123, 311-323.

825 Witte, J., Bonora, M., Carbone, C., Oncken, O., 2012. Fracture evolution in oil-producing sills of the

826   Rio Grande Valley, northern Neuquen Basin, Argentina. AAPG Bulletin 96, 1253-1277, doi:

827   10.1306/10181110152.

828 Yagupsky, D.L., Cristallini, E.O., Fantín, J., Valcarce, G.Z., Bottesi, G., Varadé, R., 2008. Oblique

829   half-graben inversion of the Mesozoic Neuquén Rift in the Malargüe Fold and Thrust Belt,

830   Mendoza, Argentina: New insights from analogue models. Journal of Structural Geology 30,

831   839-853, https://doi.org/10.1016/j.jsg.2008.03.007.

832 Zanella, A., Cobbold, P.R., Ruffet, G., Leanza, H.A., 2015. Geological evidence for fluid

833   overpressure, hydraulic fracturing and strong heating during maturation and migration of

834   hydrocarbons in Mesozoic rocks of the northern Neuquén Basin, Mendoza Province,

835   Argentina. J. S. Amer. Earth. Sci. 62, 229-242,

836   http://dx.doi.org/10.1016/j.jsames.2015.06.006.

837